Journal of Alloys and Compounds 507 (2010) 253–256

Contents lists available at ScienceDirect

Journal of Alloys and Compounds

journal homepage: www.elsevier.com/locate/jallcom

Structural investigations of nanomixed oxides SnO_2–xAl_2O_3 prepared by sol–gel technique

Z.K. Heiba [a,c,*], M.A. Ahmed [b], Sameh I. Ahmed [c]

[a] Physics Department, Faculty of Science, Taif University, Saudi Arabia
[b] Chemistry Department, Faculty of Science, Ain Shams University, Cairo, Egypt
[c] Physics Department, Faculty of Science, Ain Shams University, Cairo, Egypt

ARTICLE INFO

Article history:
Received 28 January 2010
Received in revised form 24 July 2010
Accepted 27 July 2010
Available online 4 August 2010

Keywords:
Nanostructure
Metal oxides
SnO_2–Al_2O_3
X-ray diffraction
Catalysis

ABSTRACT

Nanosize polycrystalline sample of the mixed oxides $SnO_2 + xAl_2O_3$ ($x = 0, 25, 50, 75$ wt%) were synthesized by sol–gel technique. The resulting samples were characterized with X-ray powder diffraction (XRD), differential thermal analysis (DTA) and thermogravimetric analysis (TGA). Rietveld quantitative phase analysis shows that part of alumina is incorporated into the SnO_2 lattice while the other part remains as a separate phase. For the incorporated part, some Al^{3+} are accommodated substitutionally for Sn^{3+} and some is segregated on the grain boundary surface of SnO_2. It is found that the grain size of the mixed oxides $SnO_2 + xAl_2O_3$ is below 10 nm while for pure SnO_2 it is over 41 nm, indicating that alumina can effectively prevent SnO_2 from further growing up in the process of calcination. This is confirmed by the big increase in the specific surface area for mixed oxide samples.

1. Introduction

Tin dioxide, SnO_2, is an n-type wide band gap (3.5 eV) semiconductor that presents a proper combination of chemical, electronic and optical properties that make it advantageous in several applications. The good physical and chemical properties of this oxide make it of great interest from the technological point of view for gas sensors, white pigments for conducting coatings, transparent conducting coatings for furnaces and electrodes, opto-conducting coatings for solar cells, catalysts and surge arrestors (varistors); an increasing interest in the use of anodes of SnO_2 in lithium batteries has been recently noticed [1–5]. Enhancement of these physical properties can be achieved by doping the oxide by elements of different valency. Single phase Ni-doped SnO_2 nanoparticles ($Sn_{1-x}Ni_xO_2$, with $x = 0, 0.05, 0.07$ and 0.09) has been prepared using sol–gel method [6], where Ni is claimed to replace Sn substitutionally without Rietveld structural verifications. Sulfated tin oxide as solid superacid catalyst was studied for transesterification of waste cooking oil [7]. As an anode material for lithium-ion batteries, ultra-fine tin oxide–carbon (SnO_2/C) nanocomposites gave a high capacity with good capacity retention [8] and the SnO_2 nanoparticles were embedded in the carbon matrix, with sizes between 2 and 5 nm. For tin–manganese oxide film, initial discharge capacity of 1188.3 mAh g^{-1} has been reached with very good capacity retention of 656.2 mAh g^{-1} up to the 30th cycle [9]. Applying Al-doped SnO_2 composites as the active anode material, the best electrochemical performance is achieved for 10% Al-containing SnO_2, and the electrochemical performance of this material is strongly influenced by the precursors and thermal treatment [10]. SnO_2–Al_2O_3 nanocomposites, prepared with $SnCl_2 \leq 2H_2O$ as the precursor of SnO_2 and $Al(NO_3)_3 \leq 9H_2O$ as the precursor of Al_2O_3, give the best capacitive performance with a value of 119 F g^{-1} after cycled 1000 times in comparison with the pure SnO_2 [11,12]. Saha et al. [13] reported that alumina, even without entering the lattice of SnO_2, can improve the sensitivity of SnO_2 sensors. Use of the Al_2O_3–SnO_2 as a support of Pt can improve its catalytic effect dramatically [14]. Moreover, Al–SnO_2 nanowires are promising materials for fabricating efficient emitters in the application of display devices and vacuum electronics [15].

The crystalline structure, the size and shape of the particles and the superficial characteristics are highly dependent on the followed route of synthesis. Because of the sol–gel ability to alter relative precursor reactivity, it can be used to prepare samples that are homogeneously mixed at a molecular level. Also, the ability to introduce several components into solution during the sol–gel step makes this approach especially attractive for the preparation of multicomponent oxides and bimetallic catalysts. One of the advantages of sol–gel preparation over conventional techniques is the possibility of controlling the porous structure of products, which is

* Corresponding author at: Physics Department, Faculty of Science, Ain Shams University, Abbassia, Cairo, Egypt. Tel.: +20 2 24831255; fax: +20 2 26842123.
E-mail address: zein_kh@yahoo.com (Z.K. Heiba).

0925-8388/$ – see front matter © 2010 Elsevier B.V. All rights reserved.
doi:10.1016/j.jallcom.2010.07.170

of great importance in many applications such as catalysis or ion exchange. It can be achieved not only by controlling the relative rates of hydrolysis and condensation reactions (mainly by pH) but also by controlling other sol–gel parameters.

The aims of the present work are: (i) to apply sol–gel technique for preparing nano$SnO_2 + xAl_2O_3$ polycrystalline system in ultimate to obtain nanomixed oxide with different values of x wt% and (ii) to investigate the effects of alumina on the structural and microstructural properties of stannic oxide.

2. Experimental

2.1. Samples preparation

Aluminum chloride (Prolabo) and stannic chloride (E-Merck) were used as precursor for preparing high alumina–stannia composite powder. Solutions of aluminum chloride and stannia chloride were mixed together in the required proportions to yield different SnO_2–xAl_2O_3 (x = 0, 25, 50 and 75 wt%) batches. The mixed hydrogel was obtained by drop wise addition of NH_3 hydroxide solution into the continuously stirred mixed aqueous solution of Al and Sn salt maintained at 80 °C. The viscosity of the batch gradually increased and finally set to an unblock gel at pH 8–9. The gels were then aged at room temperature for 48 h. Subsequently, the gel of each composition was washed repeatedly with distilled water to remove chloride ions and filtered. The filtered cake was oven dried. The dried gels were calcined in air in a muffle furnace at temperatures 100, 600, 900 and 1000 °C with a hold time of 2 h at the corresponding peak temperatures.

2.2. Characterization

TGA was carried out in static air using a Shimadzu AT-50 apparatus at a heating rate of 10 °C/min. DSC curves were obtained on a Shimadzu DT-30H apparatus using α-Al_2O_3 as reference material and Pt–Pt/RH thermocouple at a heating rate of 10 °C/min.

Adsorption–desorption isotherms of purified N_2 at 77 K were determined using a conventional volumetric apparatus connected to a vacuum system that allowed prior outgassing to a residual pressure of 10^{-5} Torr.

Powder X-ray diffraction data were recorded using a Philips diffractometer type X'pert MPD with Bragg-Brentano para-focusing geometry and graphite monochromated Cu Kα radiation. Data were collected over the range 2θ = 20–100° with a step of 0.03° and counting time of 4 s per step. Structure and microstructure characterization of the different samples have been made by employing Rietveld whole profile fitting method using the MAUD 2.044 software [16]. The instrumental broadening was determined with a sample of LaB_6 calibrated against a sample of NIST SRM-640b and provided by the Gem Dugout Company.

3. Results and discussion

3.1. XRD structural analysis

The XRD patterns of the system SnO_2–xAl_2O_3 with x = 0, 25, 50 and 75 wt% annealed at 1000 °C are shown in Fig. 1. Obviously the diffraction patterns of the doped samples resemble that of the pure SnO_2 except the peak at around 46.7° which belongs to Al_2O_3. This means that Al is incorporated in the SnO_2 lattice, either interstitially or substitutionally, forming a solid solution. This is confirmed by applying the search-match program where all patterns are identified as a major phase SnO_2 with casseterite tetragonal structure (ICDD card No. 41-1445) of space group $P4_2/mnm$. Even for the sample with excess alumina x = 75 wt%, the diffraction pattern of SnO_2 dominates indicating that Sn^{+4} cannot incorporate in alumina lattice.

Examining Fig. 1, one can notice the remarkable peak broadening for the doped samples compared with pure SnO_2, indicating that alumina can effectively inhibit SnO_2 crystallites from further growing up during the process of calcinations. The XRD patterns of the SnO_2–xAl_2O_3 with the weight ratio x = 25 wt% calcined at different temperatures are shown in Fig. 2. It is obvious that the diffraction peaks become narrower and stronger upon annealing at higher temperature revealing that the crystallites grow larger and the crystallinity is improved. Also, it can be seen that the sample calcined at 100 °C is in the amorphous phase, so the crystallite size can be controlled to the desired value by annealing at suitable temperature.

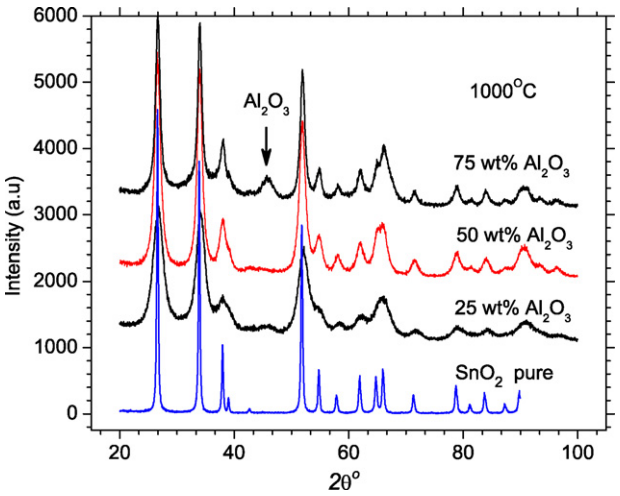

Fig. 1. XRD patterns for the system SnO_2–xAl_2O_3 (x = 0.0, 25, 50 and 75 wt%) calcined at 1000 °C.

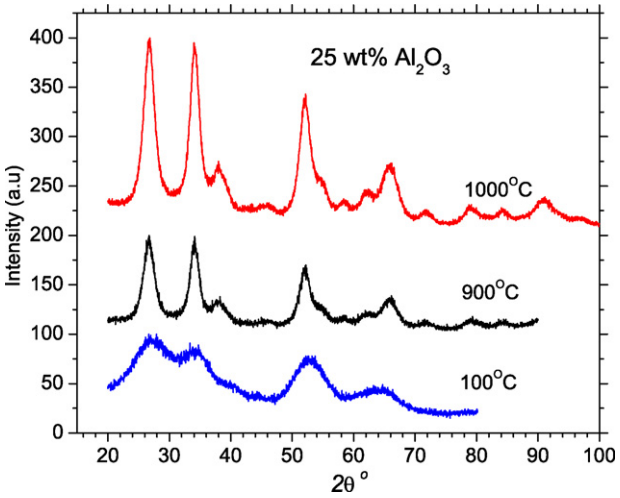

Fig. 2. XRD patterns for the system SnO_2–xAl_2O_3 (x = 25 wt%) calcined at different temperatures.

Applying the MAUD program [16], Rietveld analysis showed that part of Al^{+3} ions are incorporated substitutionally in the SnO_2 lattice replacing the Sn^{+4} ions in the position 2a. Table 1 gives the refined structural parameters obtained from Rietveld analysis. The quantitative phase analysis showed that the majority part of the Al^{+3} ions incorporated in the SnO_2 lattice, and the other part segregates

Table 1
The refined lattice parameters (a and c) (Å), the relative occupancy of Al^{+3} in the site 2a, the phase percentage of segregated α-Al_2O_3, isotropic crystallite size D nm, microstrain e and reliability factors: R_{wp} and R_p (%) obtained from Rietveld analysis of the powder XRD patterns of SnO_2–xAl_2O_3 (x = 0.0, 25, 50, 75 wt%) systems. $S_{(BET)}$ m^2/g is the specific surface area.

	x = 0.0	25%	50%	75%	100%
a	4.73789 (7)	4.7325 (5)	4.7300 (5)	4.7295 (5)	
c	3.18843 (9)	3.1752 (7)	3.1720 (5)	3.1711 (7)	
$Occ_{(Al)}$	0.0	0.21	0.32	0.33	
Seg, Al_2O_3 (wt%)	0.0	5	16	45	
D	41	8	6.5	4	
e	6^{-4}	152^{-4}	41^{-4}	34^{-4}	
R_{wp} (%)	11	5.5	6.6	8	
R_p (%)	8	4.1	4.9	6	
$S_{(BET)}$ (m^2/g)	86.5	118	196.5	214	138.3

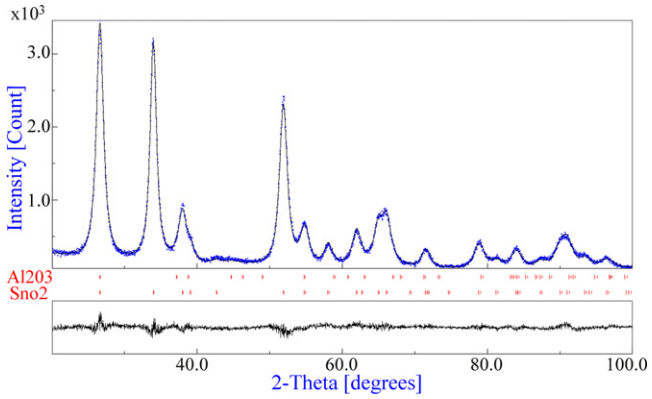

Fig. 3. The XRD profile fitting resulting from Rietveld analysis of SnO_2–xAl_2O_3 (x = 25 wt%) showing the two phases.

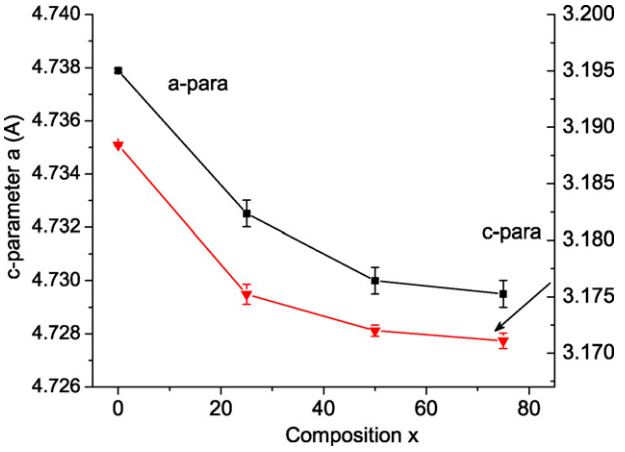

Fig. 4. Variation of the lattice parameters (a) and (c) of tetragonal SnO_2 with the weight ratio x in the composite SnO_2–xAl_2O_3.

forming a separate α-Al_2O_3 as a minor phase. Fig. 3 depicts the pattern fitting resulting from Rietveld quantitative phase analysis for the weight ratio x = 25 wt%. During refinement, the site occupancies of the cations Sn^{+4} and Al^{+3} were refined keeping the overall occupancy of the site 2a constrained to 1.0. Correlating the resulting weight percentages of α-Al_2O_3 segregated as a separate phase with the refined relative occupancies of Al^{+3} for the three doped samples, we find that they do not correspond to the weight ratios considered during preparation, some alumina is missed. This will led us to suppose that part of Al dopants is diffused on the grain boundary surface. This implies that part of the Al_2O_3 existed as a highly dispersed amorphous oxide coating on the SnO_2 nanocrystallites and suppresses the grain growth of SnO_2. Venugopal et al. [12] reported similar results for SnO_2–Al_2O_3 mixed oxides prepared by a hydrothermal method; the presence of excess Al precursor favors the formation of stannic oxide only, and in all calcined mixed oxides alumina was in amorphous phase. Without any structural analysis revealing Al accommodation, Liujiang et al. [17] illustrated that Al can effectively prevent SnO_2 from further growing up during calcination of Al–SnO_2 nanocomposite prepared by co-precipitation method. Similar results have been obtained for Mg- and Fe-doped SnO_2 [18,19] and transition metal doped SnO_2 [20].

Oxygen vacancy has very low formation energy and would commonly exist even in pure SnO_2 as predicted by Kilic and Zunger [21]. Therefore, during refinement, the occupancy of O^{-2} in the site 4f is set free to refine to allow for oxygen vacancies which is found to increase by Al^{+3} doping. This oxygen vacancy would have a direct impact on the electrical [22] and optical properties [23] of the Al_2O_3–SnO_2 system. Wang et al. [20] reported that in order to reach a more stable oxidation state, oxygen vacancies strongly attract the substitutional transition metal ions^{+3} forming transition metal–oxygen vacancy–transition metal groups. Oxygen vacancies are formed according to the equation:

$$Al_2O_3 \xrightarrow{SnO_2} 2Al'_{Sn} + V_O^{\bullet\bullet} + 3O_O^x$$

As indicated in Table 1, replacing Sn^{+4} (r = 0.71 Å) by Al^{+3} (r = 0.51 Å) reduces the cell parameters (a) and (c) but with different rates. This is shown in Fig. 4 where one can notice that the relative reduction along the c-axis exceeds that along the basal directions. Also, it is noticed that the variation is not linear as expected from Vegard's rule, because of the phase segregation of some Al ions forming α-Al_2O_3.

Inspecting the microstructural parameters given in Table 1, it is obvious that the crystallite size is highly reduced upon inserting alumina, from 41 to 8 nm which confirms the role of alumina in preventing the SnO_2 grains from growing up. No systematic change is found for the microstrain which has a little change upon doping.

3.2. Surface characterization

The specific surface area measurements of all samples are shown in Table 1. It is observed that the addition of alumina to SnO_2 increases the specific surface area of mixed oxide samples, which points to the role of alumina in preventing the small SnO_2 particles from agglomeration into large particles. This is confirmed from X-ray measurements by the big reduction in grain size for the samples doped with alumina (see Table 1). The Al_2O_3 acted as a barrier against the advancement of grain boundaries of SnO_2 and effectively prevented the grain growth and loss in surface area.

3.3. Thermal analysis

TGA and DTA were performed to determine thermal behavior of the prepared samples and hence to choose an optimum calcination temperature. Fig. 5a–c demonstrates TGA and DTA data for the systems Al_2O_3, SnO_2 and SnO_2–xAl_2O_3 (x = 50 wt%) respectively.

For alumina, the total weight loss occurs in two stages as shown in TGA (Fig. 5a). The first stage at T < 150 °C is due to removal of physically adsorbed water and results in an endothermic peak centered at 90 °C in the DSC data. The second stage involves evolution of chemically adsorbed water from the system at T > 150 °C. Since the weight loss occurs gradually during this stage, the endothermic peak is not as apparent as that of the first stage. The third stage involves dehydroxylation of aluminum hydroxide and formation of alumina oxide. The results of TGA and DSC studies indicate that heating the dried gels at temperature as low as 600 °C is sufficient to complete all reactions in the system. That is, further heating (above 600 °C) of the dried gels does not cause any thermal and/or weight changes. The total weight losses are 64 wt% for alumina.

For SnO_2, the TGA curve shows weight loss at T < 180 °C due to removal of the physical adsorbed water and which results in an endothermic peak centered at 93 °C in the DSC data (Fig. 5b). The chemically adsorbed water is removed from the system at T > 180 °C which is accompanied by removal of any chemical species in the medium of the reaction as NH^{4+} species. Like the TGA of alumina, the weight loss occurs gradually during this stage, the endothermic peak is not as apparent as that of the first stage. An exothermic peak is observed at 480 °C which is not accompanied by any weight loss in this stage and can be attributed to transformation of SnO_2 from the amorphous phase into tetragonal phase. It is obvious in Fig. 5b that above 600 °C all the reactions in the system are completed and further heating of the precipitated phases does not cause any thermal and/or weight changes. The total weight losses are 18 wt% for SnO_2.

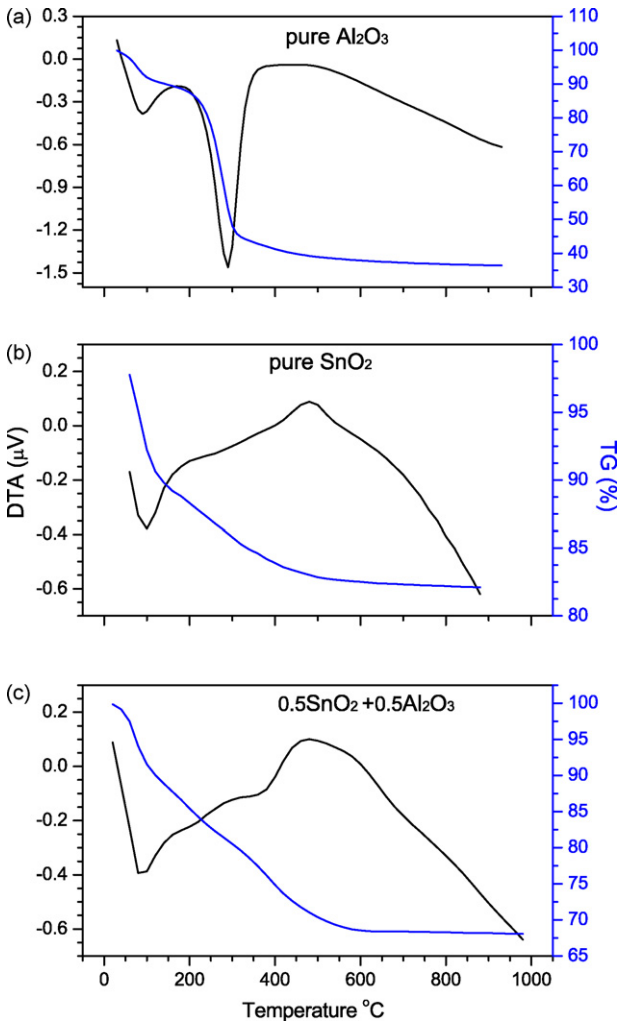

Fig. 5. DTA/TGA curves of: (a) pure alumina, (b) pure SnO_2, (c) SnO_2–xAl_2O_3 (x = 50 wt%).

The TGA and DTA curves for SnO_2–xAl_2O_3 (Fig. 5c), are very similar to that observed for SnO_2 more than that observed for alumina, with two stages observed as above. No changes upon further heating above 600 °C and the total weight losses of the sample are 32 wt%.

4. Conclusions

Nanocomposite of SnO_2–xAl_2O_3 could be synthesized applying the sol–gel technique. Part of alumina is incorporated into SnO_2 lattice and part is segregated forming a separate Al_2O_3 phase. Al_2O_3 is incorporated through two ways: some is accommodated substitutionally for Sn^{+4} forming solid solution and the remainder are deposited on the SnO_2 grain surface as a highly dispersed amorphous oxide coating on the SnO_2 nanocrystallites and suppresses the grain growth of SnO_2. Alumina plays the role of a surfactant in preventing the small SnO_2 particles from agglomeration into large particles, resulting in high specific surface area.

TGA and DTA revealed that the crystallization temperature of SnO_2 is around 480 °C and all the reactions in the system are completed before 600 °C with no changes upon further heating.

References

[1] P.G. Li, X. Guo, X.F. Wang, W.H. Tang, J. Alloys Compd. 479 (2009) 74–77.
[2] C. Wang, J. Li, Y. Zhang, YuWei, J. Liu, J. Alloys Compd. 493 (2010) 64–69.
[3] I. Matsubara, K. Hosono, N. Murayama, W. Shin, N. Izu, Sens. Actuators B: Chem. 108 (2005) 143.
[4] R.E. Presley, C.L. Munsee, C.-H. Park, D. Hong, J.F. Wager, D.A. Keszler, J. Phys. D 37 (2004) 2810.
[5] Y. Wang, X. Jiang, Y. Xia, J. Am. Chem. Soc. 125 (2003) 16176.
[6] A. Azam, A.S. Ahmed, M.S. Ansari, M.M. Shafeeq, A.H. Naqvi, J. Alloys. Compd. (2010) 184, doi:10.1016/j.jallcom.2010.06.
[7] M.K. Lam, K.T. Lee, M. Abdul Rahman, Appl. Catal. B: Environ. 93 (2009) 134–139.
[8] B. Liu, Z.P. Guo, G. Du, Y. Nuli, M. Faiz Hassan, D. Jia, J. Power Sources 195 (2010) 5382–5386.
[9] X.J. Zhu, Z.P. Guo, P. Zhang, G.D. Du, C.K. Poh, Z.X. Chen, S. Li, H.K. Liu, Electrochim. Acta 55 (2010) 4982–4986.
[10] R. Alcĭantara, F.J. Fernĭandez-Madrigal, C. Pĭerez-Vicente, J.L. Tirado, J.C. Jumas, J. Olivier-Fourcade, Chem. Mater. 12 (2000) 3044.
[11] M. Jayalakshmi, N. Venugopal, K.P. Raja, M.M. Rao, J. Power Sources 158 (2006) 1538.
[12] N. Venugopal, K.P. Raja, C.K. Chakravarthi, M. Jayalakshmi, M.M. Rao, Mater. Res. Innov. 12 (3) (2008) 127–133.
[13] M. Saha, A. Banerjee, A.K. Halder, J. Mondal, A. Sen, H.S. Maiti, Sens. Actuators B: Chem. 79 (2001) 192.
[14] D.B. Adriana, G.R. Claudia, R.D. Sergio, A.S. Osvaldo, Catal. Today 133–135 (2008) 28–34.
[15] L.A. Ma, Y. Ye, L.Q. Hu, K.L. Zheng, T.L. Guo, Physica E 40 (2008) 3127–3130.
[16] L. Lutterotti, Maud 2.044, http://www.mg.unitn.it/~Luttero/maud.
[17] X. Liujiang, Q. Dong, H. Xiaohong, W. Hong-En, J. Alloys Compd. 462 (2008) 42–46.
[18] H.R. Ricardo, J.P. Gilberto, D. Gouv, Appl. Surf. Sci. 253 (2007) 4581–4585.
[19] F. Limei, Z. Xiaotao, L. Chunming, L. Zhijie, P. Germanas, Z. Sha, L. Huakun, W. Lumin, J. Alloys Compd. 491 (2010) 679–683.
[20] X.L. Wang, Z.X. Dai, Z. Zeng, J. Phys.: Condens. Matter 20 (2008) 045214.
[21] K. Cetin, Z. Alex, Phys. Rev. Lett. 88 (2002) 95501.
[22] M.-M. Bagheri-Mohagheghi, M. Shokooh-Saremi, J. Phys. D: Appl. Phys. 37 (2004) 1248–1253.
[23] D. Chen, L. Gao, J. Colloid Interface Sci. 279 (2004) 137–142.